Optimised design of screw anchors in tension in sand for renewable energy applications

Benjamin Cerfontaine*, Jonathan Knappett, Michael John Brown, Craig Davidson, Yaseen Sharif

ABSTRACT

The offshore deployment of floating offshore structures such as wind turbines or wave energy converters is expected to strongly increase during the next decade, to face the appetite for green energy sources. The growing size of these structures' dimensions, inducing very large mooring forces, makes the anchoring solution adopted a critical issue for the commercial success of floating marine energy farms.

The upscaling of the screw anchor technology from onshore to the offshore environment has been recently proposed as an efficient way of providing a large tension capacity while their installation generates far less noise and vibrations than impact pile driving. Most of recent studies on screw anchors have focused on separated geotechnical problems such as their uplift capacity or installation requirements. This paper incorporates within a single procedure geotechnical and structural constraints to calculate the optimal anchor geometry able to maximise the uplift capacity available.

Performance envelopes for screw anchors have been derived in a parametric study, covering a broad range of soil conditions as well as in a case study, representative of offshore conditions. Results show that single screw anchors are more efficient (e.g. shorter and lighter) than driven piles to sustain tension loading. The results presented in this study support the applicability of screw anchors to be used as part of the mooring system for wave energy converters. However, tension requirements for tension-leg platform wind turbines would probably require the use of group of anchors.

KEYWORDS

Screw anchors; Anchor design; Offshore Geotechnics; Renewable Energy

1. INTRODUCTION

Current research in offshore geotechnical engineering concerning foundations and anchoring is dominated by the lateral loading, e.g. for monopiles (Burd et al., 2019) or for catenary mooring systems (Fontana et al., 2018). However, some floating or fixed-bottom structures generate significant vertical tension on their foundations/anchors, as shown in Figure 1. This figure summarises tension capacity requirements for offshore foundations, obtained from the literature for specific case studies, derived from analytical, experimental or numerical assessment.

Tension-leg platforms for the Oil & Gas industry (Randolph and Gourvenec, 2011) have large tension requirements (up to 17MN for a jacket, but up to 240MN for a group of anchors for tension-leg platform) while tension-leg floating wind turbines (Bachynski and Moan, 2012; Oguz et al., 2018) require an uplift capacity in the range of 8-18MN per fairlead (connection between the mooring line and floating structure). Jacket (Davidson et al., 2019) or tripod (Byrne and Houlsby, 2015) fixed structures for offshore wind turbines resist large overturning moments through push-pull action (i.e. compression/tension load, of the order of 10-20MN). Wave energy converters vary in size, but the largest may require a vertical capacity of several MN (Gaudin and O'Loughlin, 2018; Herduin et al., 2018) due to the inclination of taut mooring lines or consist of a single point absorbed with a single vertical mooring line (Vicente et al., 2013a). In contrast, floating net-cage systems used in aquaculture also require an engineered anchoring solution for offshore deployment in exposed waters (Huang et al., 2008), although typically of a lower order of magnitude (~0.2MN).
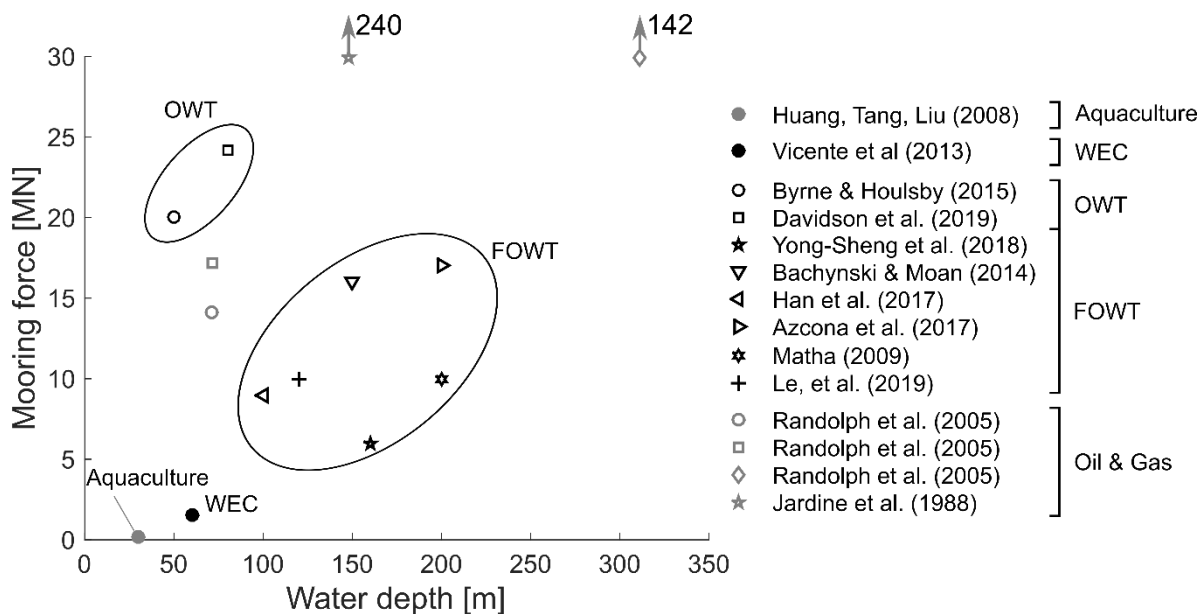

Figure 1 Tension capacity requirement as a function of the water depth for aquaculture, wave energy converters (WEC), bottom-fixed offshore wind turbines (Fixed OWT), floating wind turbines (Floating OWT) and Oil & Gas industry applications (installed -group- anchor capacity)

Pile and suction anchors are common solutions to resist purely vertical tension loading (Aubeny, 2017). However, they resist such actions principally through the mobilisation of friction along their shaft and their own self weight, which may not be very efficient. The installation of suction caissons in some soil profiles (e.g. in coarse-grained soils) may also prove complicated (Sturm, 2017) and expensive per foundation unit (Aubeny, 2017). Suction embedded plate anchors (SEPLA) or dynamically embedded plate anchors (DEPLA) are two recently developed installation methods allowing the deployment of plate anchors, although their installation is mainly restricted to cohesive soils.

Onshore screw or helical anchors have been widely used to found light structures or anchor communication towers (Clemence and Lutenegger, 2015; Perko, 2009a). They are composed of one or several steel helices attached to a central core (or shaft). They are installed into the soil through the application of a torque and a compression (or 'crowd') force at their top. Screw anchors have recently been proposed for offshore applications (Al-Baghdadi et al., 2017a; Byrne and Houlsby, 2015; Davidson et al., 2018b) as they have several advantages in addition to their high uplift capacity, including reduced environmental impact (as low vibrations or sound are generated during their installation), an ability to be easily removed by applying torque in the opposite direction (design for decommissioning) and ability to be installed in varied soil conditions. As a downside, screw anchors are more complicated to manufacture than a straight shafted pile, although relatively large geometries (D_h =0.76m) have already been used for bridge foundations (Harnish et al., 2017) demonstrating the feasibility of this technology. They also require the development of new tools for their installation offshore to provide the large torques required for installation.

The literature on screw or helical anchors is mainly focused on the study of relatively small diameter (<0.5m) helices (El Sharnouby and El Naggar, 2012; Li et al., 2018; Sakr, 2009; Tsuha et al., 2007). However, their use as offshore foundations will require a significant upscaling of the anchor dimensions to resist vertical loads of several MN (as shown in Figure 1), but also lateral loading (Al-Baghdadi et al., 2017a; Cerfontaine et al., 2019a; Davidson et al., 2019; Hong-yan et al., 2018).

To date, the torque required for the installation of screw anchors has mainly been investigated using correlation factors (K_T) which have previously been proposed to empirically estimate the uplift capacity from the measured installation torque (Ghaly et al., 1991; Harnish et al., 2017; Tsuha and Aoki, 2010) and vice versa. However, recent studies have shown that the torque, as well as crowd force, necessary to install such screw anchors might pose a significant hurdle for their use offshore (Al-Baghdadi et al., 2017b; Davidson et al., 2019) and require accurate estimations for varying pile geometries in different soil types.

Many different uplift capacity calculation methods have been developed for plate and screw anchors, all based on an assumed failure mechanism (Cerfontaine et al., 2019b). This mechanism is usually considered as deep or shallow based on the helix relative embedment ratio (H/D_h) (Meyerhof and Adams, 1968; Mitsch and Clemence, 1985), where H is the height of soil above a buried helix and D_h is the helix diameter. The approach proposed by Giampa et al. (2017) considers that where a shallow failure mechanism occurs it has the shape of a truncated cone whose lower base is formed by the upper-most helix, as shown in Figure 2(a). This approach has been shown to be consistent with centrifuge tests in independent studies with and without installation effects (Cerfontaine et al., 2019a; Hao et al., 2019).

While many previous studies have addressed geotechnical issues (e.g. capacity and installation requirements), relatively few have tried to identify the load distribution in the anchor structural elements (Papadopoulou et al., 2014; Schiavon et al., 2017), its structural design or practical construction. The objective of this work is to derive a methodology enabling a rapid optimisation of screw anchor design in sand and the identification of the achievable performance envelope, considering installation, capacity and structural constraints.

The originality of this work lies in the combination of the structural and geotechnical constraints for the optimisation of upscaled screw anchors for offshore applications. While for most onshore applications, the installation and structural requirements can mostly be met, these requirements limit the available capacity for offshore applications. In addition, the bending moment in the helix was explicitly investigated and compared with the analytical approach adopted in the following, which is usually neglected. This paper presents a holistic design method combining all geotechnical and structural constraints. The method enables the determination of a quick design chart, identifying the maximum capacity that can be achieved

3

for an optimised anchor geometry for given soil conditions. Finally, a comparison between the uplift capacity of anchors and driven piles for a case study has been proposed for the first time, quantifying the advantages of screw anchors.

The soil-structure interaction is firstly analysed, based on numerical modelling results validated against centrifuge tests, to identify the load distribution and bending moment acting on the helix during uplifting. The different structural and geotechnical constraints limiting the uplift capacity are then defined based on simplified procedures informed by the soil-structure interaction results. The procedure is illustrated through a parametric study to define the performance envelope of screw anchors in three sandy soil conditions. Finally, the efficiency of screw anchors is demonstrated by comparison with driven straight piles in tension for a case study in Dunkirk sand.

2. SOIL STRUCTURE INTERACTION

The following section illustrates how a more accurate understanding of the soil-structure interaction between the soil and the anchor can be used to identify suitable design loads. A schematic free body diagram of a shallow anchor embedded in sand is represented in Figure 2(b). It is assumed that the shallow failure mechanism resulting from the application of the vertical load F_y is a truncated cone whose base is in contact with the helix (Giampa et al., 2017). To ensure the force equilibrium of the soil wedge, the shear stress distribution along the failure mechanism (τ_{soil}) must be balanced by the internal normal distribution acting on the helix (σ'_N) and shear stress distribution along the core (τ_c).
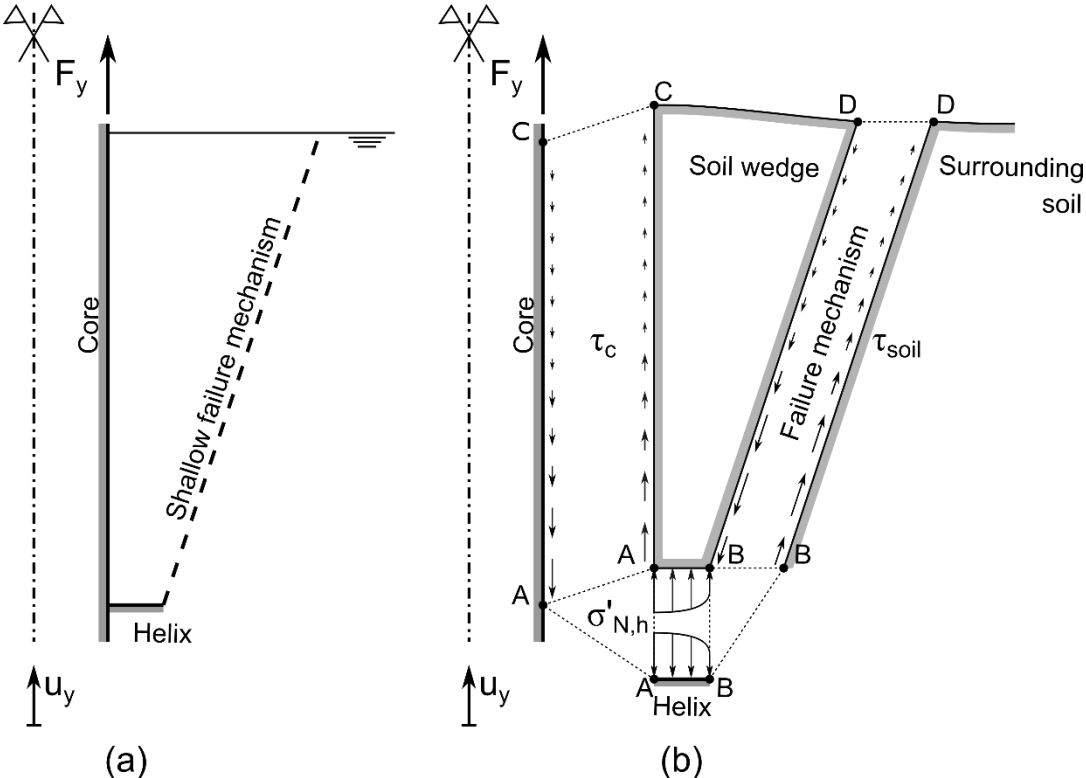

Figure 2 (a) Sketch of the anchor geometry and assumed failure mechanism. (b) Free body diagram of the soil-screw anchor system (shear stress along the helix and normal stress along the failure mechanism and the core are not represented for clarity)

A 2-step approximate numerical procedure (using the Finite Element software PLAXIS (2017)) has been previously established and validated against centrifuge tests to simulate the load-displacement relationships of screw anchors (Cerfontaine et al., 2020) under monotonic uplift loading, accounting for the effects of installation on the stress field within the soil. The

4

behaviour of a particular anchor (helix diameter 1.7m, core diameter 0.88m, relative embedment ratio 7.4) embedded in dense sand (Relative Density, D_r = 84%) and described in detail in (Cerfontaine et al., 2020; Davidson et al., 2019) is given below as an example. The helix is idealised as a horizontal plate attached to the shaft, which has been proven experimentally (Hao et al., 2019) and numerically (Al-Baghdadi, 2018) to be a good approximation.

The soil was modelled by the hardening soil constitutive law with small strain deformation (Schanz et al., 1999), which has been widely used and calibrated at the University of Dundee (Al-Defae et al., 2013; Cerfontaine et al., 2019b; Knappett et al., 2016) for the HST95 sand as a reference and utilised in previous screw pile studies. The steel pile was modelled by plate finite elements based on the Reissner-Mindlin theory (Zienkiewicz and Taylor, 2000). The soil-structure interaction was controlled by interface finite elements with a Mohr-Coulomb constitutive model. The mesh was composed of triangular 15-node elements (PLAXIS, 2017) whose size is refined close to the anchor. The details of the modelling can be found in Cerfontaine et al. (2020).

The comparison of the numerical (Num.) and centrifuge (Exp.) vertical load F_y versus vertical displacement u_y relationship is depicted in Figure 3(a). The total load acting at the head of the anchor obtained numerically slightly overpredicts the capacity obtained experimentally, defined as the maximum vertical load. The stiffness of the anchor (relevant for hydrodynamic studies of floating system performance at working load) can also be determined to a high level of accuracy. Figure 3(b) shows that at low uplift displacement, the share of the load carried by the helix is much larger than that carried by the anchor's core. Both load components increase with increasing uplift displacement, but the relative load sharing between the helix and the core decreases and increases respectively. A similar trend was observed for two other simulations (Cerfontaine et al., 2020), but not presented here) that were also validated against centrifuge data (an anchor at lower H/D_h in dense sand and medium-dense sand respectively), although the magnitudes of load carried by the helix (and core) were different at failure (75% of the total capacity was sustained by the helix in medium-dense sand).

Figure 4 shows the axial load distribution within the plate finite elements simulating the anchor core, for the simulation shown in Figure 3. The jump clearly visible at 12.5m depth represents the connection of the helix to the core. The magnitude of this jump represents the load carried by the helix. The core share is calculated as the difference between the total load measured at the top of the anchor and that at the helix depth. Figure 4 indirectly shows that the stress distribution along the core is non-linear. Indeed, the core load at failure increases rapidly close to the helix up to approximately two helix diameters above the helix (i.e. between 12.5m and 8m) and is approximately constant above this. Identifying the normal stress distribution acting on the helix will prove important in the following design optimisation, as these loads induce bending of the helix plate that must be limited to avoid structural failure. The redistribution of stress between the shaft and the helix, and shear stress enhancement close to the helix have already been observed for a different type of anchor (tie-rod and extruding sockets) by Pisano and di Prisco (2014).
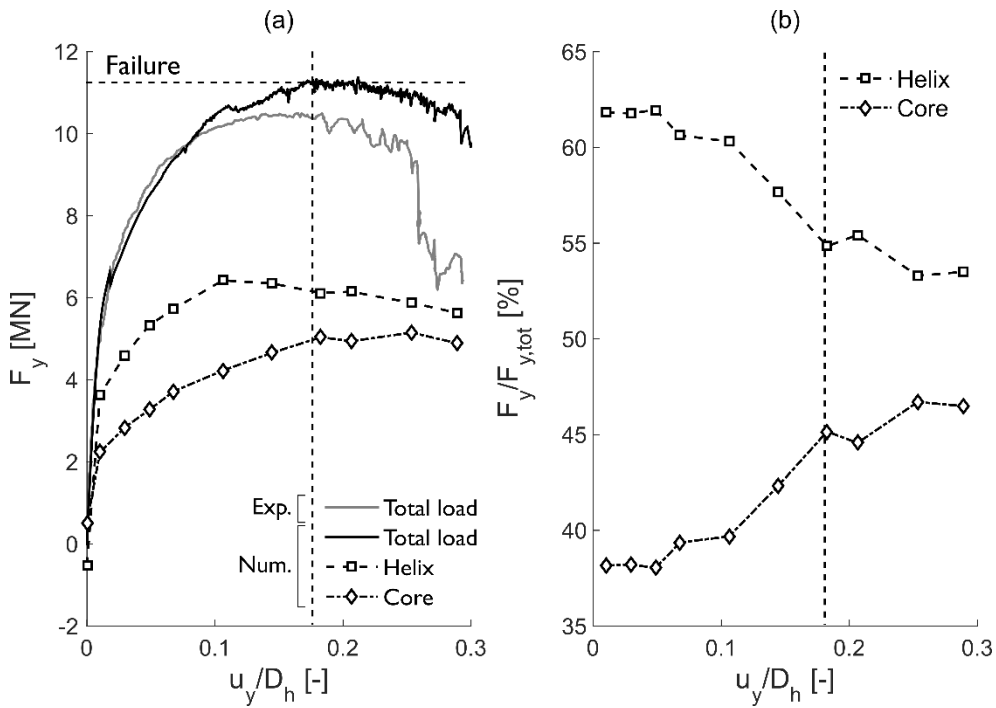
5

Figure 3 (a) Comparison of the uplift load (F_y) -displacement (u_y) relationship obtained through finite element simulations and decomposition between helix and core shares for a screw anchor embedded in dense sand at a relative embedment depth equal to H/D_h=7.4. (b) Relative shares of the load carried by the helix and the core with respect to the total uplift load.
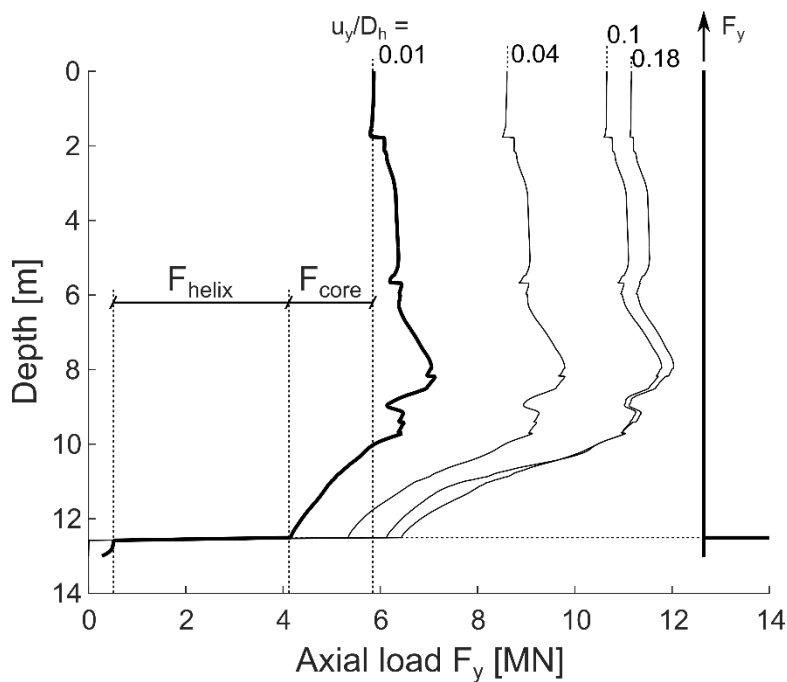

Figure 4 Axial load distribution F_y within the core of an anchor embedded in dense sand at a relative embedment ratio equal to 7.4. Annotated to show the indicative contributions at u_y/D_h = 0.01, 0.04, 0.1 and 0.18.

6

3. SIMPLIFIED DESIGN APPROACH FOR ANCHOR SIZING

3.1. Screw anchor geometry

The anchors considered here are composed of a core and a single helix, as shown in Figure 5. The anchor core is defined by its diameter D_c, its wall thickness t_c and its length H, which is assumed identical to the embedment depth of the helix mid-plane. The actual length of the core will probably be slightly longer in practice, for instance to ensure competent connection of the helix to the core through welding and/or addition of a particular tip design. The helix is characterised by its diameter D_h, its plate thickness t_h (not necessarily constant over the helix) and its pitch p_h. All of these dimensions are considered as design variables in the following optimisation, except for the pitch dimension, which is kept constant and equal to $D_h/3$. This dimension is within the range typically found within documented field studies ($0.15D_h$-$0.33D_h$) as summarised in Cerfontaine *et al.* (2019a) which may have arisen empirically to take account of larger soil units to avoid clogging of the helix.
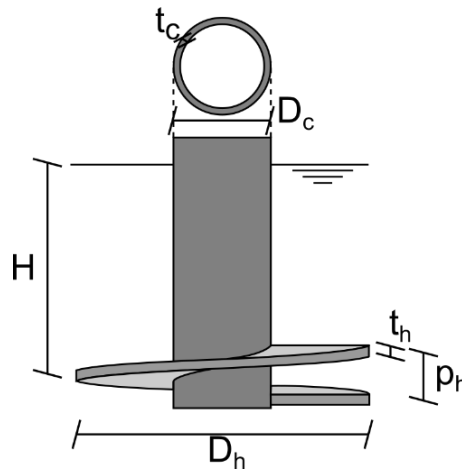

Figure 5 Schematic of the single helix anchor geometry where D_c core diameter, t_c core thickness, D_h helix diameter, t_h helix thickness, p_h helix pitch and H helix embedment (Note the width to length ratio is exaggerated in the schematic).

3.2. Installation requirements

A torque is applied at the top of the anchor core to screw it into the ground. In practice, it is recommended that the penetration rate of the anchor must be equal to one helix pitch p_h per helix rotation (Perko, 2009b), to ensure a true helical movement (referred to as pitch matched or perfect installation) and limit soil disturbance. Subsequently, a vertical compression (crowd) force must be applied accordingly to enforce this vertical displacement.

A method has been developed and validated against centrifuge tests (which maintained an installation of one helix pitch penetration per helix rotation) to estimate the force and torque requirements with depth, based on Cone Penetration Test (CPT) in-situ test data (Davidson et al., 2020, 2018a). A thorough comparison between several prediction methods and centrifuge tests has been undertaken by Davidson et al., (2020).
The torque $T(H)$ can be decomposed into several components related to the core T_c, to the base T_b, and to the helix T_h. Each component is calculated independently as a function of geometrical variables, CPT results and interface properties:

$$T(\mathrm{H}) = T_c(D_c^2, \bar{q}_c(H), a, \mathrm{H}) + T_b(D_c^3, \bar{q}_c(H), \delta_{crit}) + T_h(D_h^3, D_c^3, \bar{q}_c(\mathrm{H}), a, t_h, K_0) \qquad (1)$$

where $\bar{q}_c(z)$ is the averaged cone resistance q_c over $z = H \pm 1.5D_h$, δ_{crit} is the critical sand-steel interface friction angle and K_0 is the coefficient of lateral earth pressure at rest based on the sand critical state friction angle (ϕ_{crit}) through the Jaky formula (Jaky, 1944). The stress

7

drop index a (Lehane et al., 2005) is used to calculate the lateral stress acting on the anchor and defined as $F_r/\tan\delta_{crit}$, where F_r is the CPT friction ratio. The crowd force $F_{y,c}(z)$ can be estimated following a similar methodology

$$F_{y,c}(\text{H}) = F_c(D_c, \bar{q}_c(H), \delta_{crit}, \text{H}) + F_b(D_c^2, \bar{q}_c(H)) + F_h(D_h^2, D_c^2, \bar{q}_c(\text{H}), t_h, K_0) \qquad (2)$$

The detailed equations of the method are provided in section 10.

The force and torque required to install an anchor whose helix diameter D_h is equal to 1.5m in dense sand (D_r = 82%) is given in Figure 6 as a function of the installation depth *H* for several core diameters D_c. These values might become very large as depth increases, limiting the practical achievable embedment of the helix as a function of the installation equipment that is available. For instance, one of the largest current onshore installation devices, the 'silent piler GRV2540' is able to install straight piles up to a diameter of 2.5m with a maximum torque equal to 3MNm (Giken, 2018). However, the offshore industry has already demonstrated its capabilities to upscale traditional technologies and installation techniques, e.g. monopiles have grown from a couple of meters in diameter to almost 8m for the most recent wind farms (Negro et al., 2017).

The magnitude of the compression force $F_{y,c}$ calculated in Eq. (2) is extremely large, which can be a limiting factor for the installation of screw anchors. However, one of the hypotheses of the force prediction method is that the screw anchor has a flat solid base or is fully plugged during its installation. Consequently, the major contribution to the total force $F_{y,c}$ is the base component F_b. In practice the rotary jacking installation of an open-ended anchor will reduce the plugging effect (Deeks et al., 2010), decreasing the total compression load at the base. The use of a pointed tip for a close-ended anchor will also decrease this required compression load. Therefore Eq. (2) is an upper bound for practical applications.
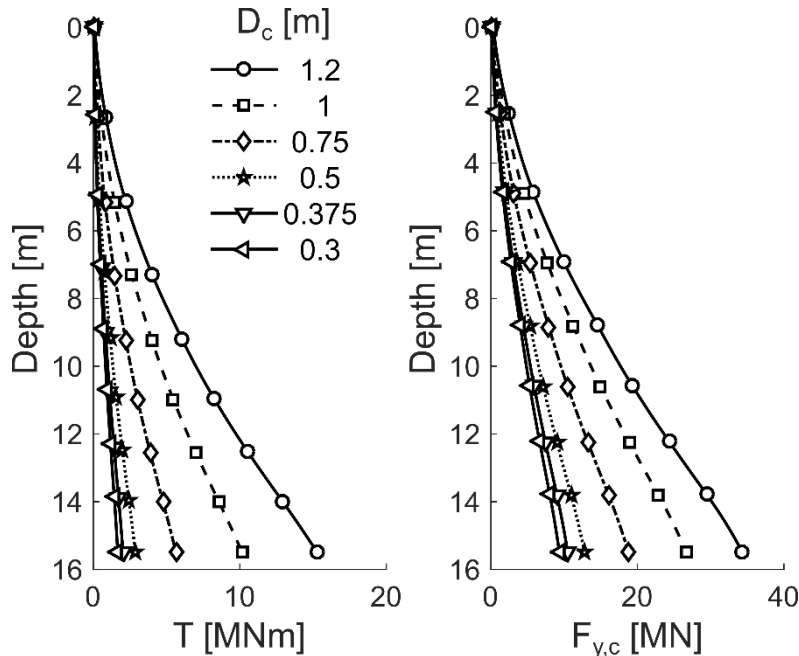

Figure 6 Torque *T* and force $F_{y,c}$ requirement associated with the installation of an anchor (D_h = 1.5m) in dense sand (D_r = 82%) for different core diameters D_c. The corresponding soil parameters are given in Table 2 and the corresponding CPT data in Figure 12.

3.3. Core section structural requirements

The core section must be able to resist the combined shear and normal stresses resulting from the crowd force and torque application during the installation. In the different cases considered below, this combined load in the core is always more severe during installation than during uplifting (service). Therefore, the core section verification is undertaken only for the installation phase. The installation torque T generates a circumferential shear stress τ in the annular core such that the maximum shear stress is obtained from

$$\tau = 16 \frac{T}{\pi} \frac{D_c}{D_c^4 - (D_c - 2t_c)^4} \tag{3}$$

which converges towards Bredt's formula at low wall thickness. In addition, the vertical crowd force generates a vertical normal stress σ_y inside the section such that

$$\sigma_y = \frac{4}{\pi} \frac{F_{y,c}}{(D_c^2 - (D_c - 2t_c)^2)} \tag{4}$$

The equivalent Von Mises stress $\sigma_{eq,c}$ is then calculated to verify that the yield limit of the steel core section f_y is not exceeded:

$$\sigma_{eq,c} = \sqrt{\sigma_y^2 + 3\tau^2} \leq f_y \tag{5}$$

In addition, there is a limitation on the core wall thickness t_c, to ensure it is practically possible to manufacture it. It is assumed to be no larger than 10% of the core diameter D_c and lower than 100mm in any case. This is in accordance with thick pile dimensions that can be found in various manufacturers' catalogues, e.g. (JFE, 2019).

The compression force within the core increases with the anchor length and helix embedment. Consequently, there is a risk of buckling of the core, which is only partially restrained at its tip. Solving the buckling problem of partially embedded piles is complex (Gabr et al., 1997; Heelis et al., 2004). Therefore, a simplified approach was adopted. The rotation and lateral displacement restraint at the anchor tip increase with depth as the lateral stress and stiffness within the soil increase, as show in Figure 7(a). In addition, the helix restrains the rotation of the pile with respect to its neutral axis. Therefore, the critical elastic load within the pile $F_{y,cr}$ was calculated based on the assumption that the base of the anchor was clamped, but the top of the core is free to rotate and move laterally, as depicted in Figure 7(b). Therefore, the formula for the first mode elastic buckling of a column was considered using Euler's well-known Euler equation

$$F_{y,cr}(H) = \pi^2 \frac{EI}{(KH)^2} \geq F_{y,c}(H) \tag{6}$$

where E is the Young's modulus of the core and I is its second moment of area. The coefficient K depends on the support conditions of the column, e.g. a cantilever column in this case ($K = 2$). For a given embedment depth of the anchor, the critical buckling load $F_{y,cr}(H)$ must be larger than the crowd force $F_{y,c}(H)$ required to install it at this depth. This approach is very conservative as the soil around the core will provide additional restraint against buckling, as previously shown (Heelis et al., 2004). However, the method's main advantage is its simplicity and that it does not require any additional data. Local buckling of the core wall is not investigated as the hollow closed sections are of class 1-3 as defined in (Eurocode, 2005).
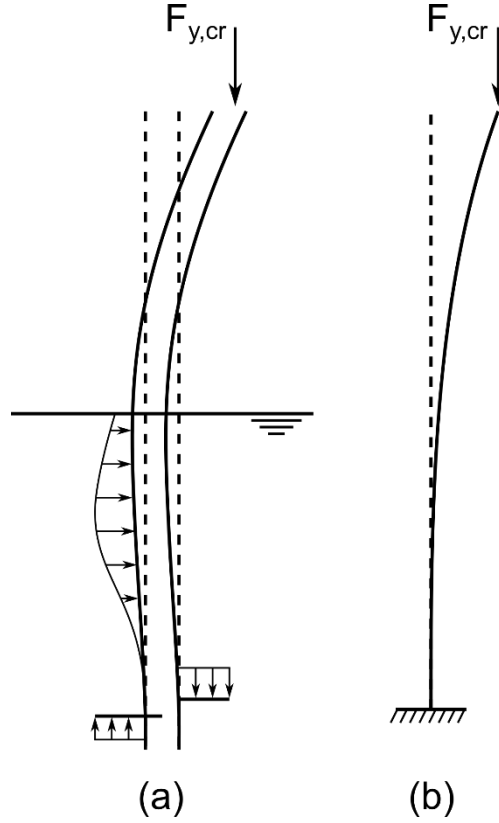
Figure 7 Idealisation of the screw anchor buckling (a) with a partial soil restraint, (b) as a base clamped problem

3.4. Uplift capacity (geotechnical performance requirements)

The uplift capacity F_u of plate and screw anchors in coarse-grained soils is mostly dependent on the failure mechanism developed within the soil. Many methods have been proposed to assess the capacity of these anchors, as summarised in (Cerfontaine et al., 2019b). The approach proposed by (Giampa et al., 2017), assuming a shallow failure mechanism that develops from the edge of the anchor up to the surface, inclined at the angle of dilatancy ψ to the vertical, was found to be consistent with centrifuge tests of different anchor geometries and soil conditions from the literature (Cerfontaine et al., 2020; Hao et al., 2019):

$$F_u = \left[1 + F_{s1} \frac{H}{D_h} + F_{s2} \left(\frac{H}{D_h} \right)^2 \right] \gamma' \frac{\pi}{4} D_h^2 H \qquad (7)$$

$$F_{s1} = 2F_{ps} \qquad (8)$$

$$F_{s2} = \frac{4}{3} F_{ps} \, tan \, \psi_p \qquad (9)$$

$$F_{ps} = tan \, \psi_p + cos \, (\phi_p - \psi_p)(tan \, \phi_p - tan \, \psi_p) \qquad (10)$$

where $F_{s,1}$, $F_{s,2}$ and $F_{p,s}$ are uplift factors, ϕ_p and ψ_p and the sand peak friction and dilatancy angles and γ' is the buoyant sand unit weight. These equations result from the weight of the shallow wedge of soil moved upwards above the helix and the integration of the shear stress mobilised along the failure mechanism that develops minus the vertical component of the normal stress. F_{ps} is the uplift factor for plane strain conditions initially defined by White et al. (2008) and modified for axisymmetric conditions by Giampa et al. (2017). The normal and

shear stress mobilised on the failure surface are assumed to decrease linearly with depth up to the surface.

Initially, the method represented by Equations (7)-(10) was developed for anchors whose relative embedment ratio H/D_h was limited to 5 (Giampa et al., 2017). Results of recent centrifuge tests have shown that this approximation of uplift capacity is still appropriate up to H/D_h equal to 7.4 (Cerfontaine et al., 2019a). However, the displacement required to fully mobilise the failure mechanism increases with depth. It lies between $0.1D_h$ and $0.2D_h$ at H/D_h equal to 7.4, while $0.1D_h$ is sometimes used as a practical limit used to define the anchor failure (Sakr, 2009). Therefore, it has been decided herein to limit the maximum relative embedment ratio H/D_h to 8, in order to ensure Eq. (7) is still valid (shallow mechanism) and the displacement at failure remains limited to acceptable values.

3.5. Helix bending

A significant load acts on the helix during both the installation and the anchor uplift generating a bending moment at the helix-core connection. The helix is idealised as a plate clamped to the central core with a full moment fixity (i.e. no rotation while within the elastic range), as shown in Figure 9. For a given depth, the uplift load is calculated through Eq. (7) while it is possible to identify the load acting on the helix during installation based on Eq. (2). The maximum of these two loads, $F_{y,max}$, is used to calculate the maximum bending moment. As a first approximation, it is assumed the maximum load is transferred through the helix as a distributed constant load q such that

$$q = \frac{4F_{y,max}}{\pi(D_h^2 - D_c^2)} \tag{11}$$

The maximum horizontal stress resulting from the bending moment in the helix plate is obtained through the approach proposed by Timoshenko and Woinowky-Krieger (1959)

$$\sigma_x = k\frac{qD_h^2}{4t_h^2} \leq f_y \tag{12}$$

where k is a constant that depends on the D_h/D_c ratio and varies as reported in Table 1. In addition, it is assumed that the maximum helix plate thickness is limited to 100mm at the helix-core connection. Although the helix thickness could be variable in practice, it is assumed constant in this case.

D_h/D_c [-]	1.25	1.5	2	3	4
k [-]	0.135	0.410	1.04	2.15	2.99

Table 1 Coefficient k as a function of D_h/D_c, (Timoshenko and Woinowky-Krieger, 1959)
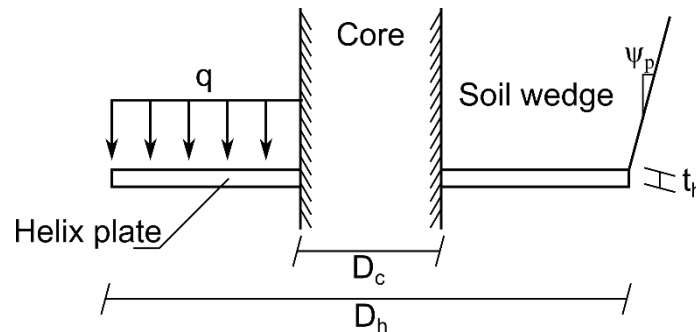

Figure 8 Idealisation of the shallow failure mechanism and helix bending

The actual distribution of normal stress acting on the helix plate for the simulation presented in section 2 is represented in Figure 9(a) at given values of u_y/D_h. Results correspond to the finite element simulation presented in Section 2. The normal stress is a maximum at the helix-core connection and decreases non-linearly to zero at the edge of the helix plate. The actual maximum normal stress observed numerically is always lower than the uniform stress considered in Eq. (11), which assumes that the entire uplift capacity is sustained by a vertical load applied onto the helix. In reality, only a fraction of the total capacity is actually transferred to the core through shearing, as described in section 2, leading to a lower loading of the helix.

Similarly, the bending moment at the helix-core connection obtained as a direct result from the horizontal plate finite elements for the simulation presented in section 2 (hereafter termed 'Plate FE result') is depicted in Figure 9(b), as a function of the uplift displacement. It is compared to the bending moment obtained through Eq. (12) by considering either the total uplift load (F_y) acting on the helix at a given value of u_y/D_h (Eq. (11)) or the ultimate capacity (F_u, in Figure 9) calculated through Eq. (7). Results show that the analytical approach overpredicts the bending moment in the plate, which is conservative. In addition, the design approach can accommodate a possible load redistribution between the shaft and the helix during cyclic loading, as discussed in (Schiavon et al., 2016).
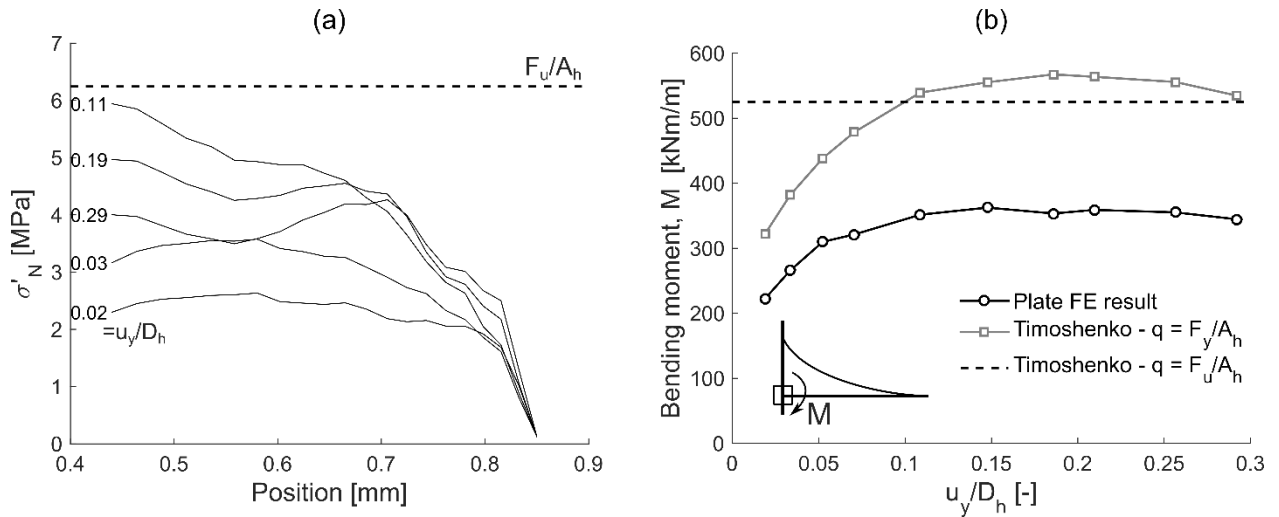

Figure 9 Uplift simulation of an anchor (D_c = 0.88m, D_h = 1.7m) embedded in dense sand (D_r = 84%). (a) Normal stress distribution acting on the helix plate for relative displacement u_y/D_h equal to 0.02, 0.03, 0.11, 0.19 and 0.29. (b) Evolution of the bending moment M at the helix-core connection with vertical uplift displacement.

It is assumed that the connection between the helix and the core consists of two weld joints, as depicted in Figure 10(a). It is further assumed that the shear load is evenly split between the two weld joints, while the moment is resisted through a couple of horizontal forces F of equal magnitude and opposite direction, as shown in Figure 10(b). The normal and shear stress acting along the weld throat a_w (Figure 9(c)) are calculated to balance these two loads and the section strength is calculated through the Von Mises criterion (see Appendix) (EN1193-1-8, 2005).

In all cases considered in this paper, it was observed that if a sufficiently large weld throat can be achieved (no more than 35mm) and the yield strength of the joint is equal to that of the helix, the plate bending criterion is often more detrimental than the connection. This is valid for the case of monotonic loading and does not consider a possible fatigue effect within the welded joints. The true helix shape, which is different from a plate, could also create a more complex stress distribution at the connection.

A recent 1-g experimental study has demonstrated that the compression bearing capacity of screw piles which have undergone permanent helix bending were lower than undeformed piles (Malik et al., 2019). This phenomenon was due to a modification of the soil movement around the deflected helix. This is not considered in the present case because the criterion adopted for the helix bending ensures no yielding of the helix occurs. Consequently, there is no permanent deflection of the helix. In addition, the loading applied in tension is lower than in compression, as shown for instance in (Davidson et al., 2019; Sakr, 2009).
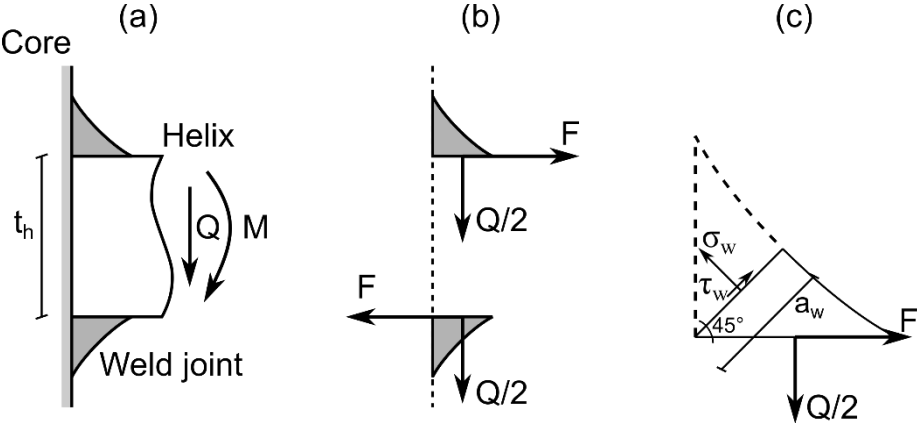

Figure 10 Loading of the weld joint (a) Bending moment M and shear load Q that must be transferred to the core (b) Loads acting on the weld joints (c) Stress state along the upper weld throat a_w

4. PARAMETRIC STUDY

4.1. Optimisation procedure

The objective of this section is to define a performance envelope of screw anchor uplift capacity, given a maximum torque that can be provided during installation, in a given set of soil conditions representative of offshore conditions. The maximum capacity depends on the geometry of the anchor and the maximum embedment depth of the helix. This maximum embedment depth is limited by the potential constraints previously defined.

Subsequently, the methodology consists of systematically varying the helix diameter D_h and the helix to core diameter ratio D_h/D_c and finding the maximum embedment H that can be achieved with respect to all of the different possible constraints. The implementation consists of several embedded loops, as depicted in Figure 11. For a given soil density, the maximum torque available for installation is varied. For each geometry considered, the maximum embedment depth is calculated as well as the capacity. The procedure is illustrated through some examples detailed in sections 4.3 and 4.4 and the final results are given in section 4.5. The procedure which follows does not include any factors of safety, as partial safety coefficients vary from one design code to the other. A suitable factor of safety can be applied to the anchor resistance as a whole (DNV-GL, 2018).
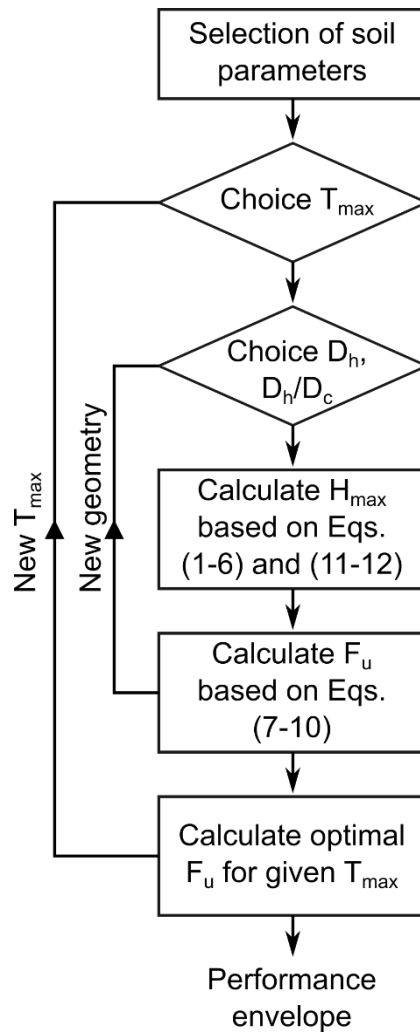
Figure 11 Flow chart of the optimisation procedure

4.2. Soil conditions

Many offshore wind projects are developed in the North Sea, where sand seabed conditions are very common (Bjerrum, 1973). Medium-dense to very dense sand layers are often encountered, e.g. for two recently built wind farms (Le et al., 2014; Merritt et al., 2012). Consequently, three sand densities (loose, medium and dense) were considered in this parametric study to cover a wide range of soil conditions.

In the following, the screw anchor is assumed to be embedded in a synthetic homogeneous sand layer of constant density. A set of parameters determined for the HST95 sand is used, for which CPT tests are available for three different densities (D_r = 38, 52 or 82%) representing loose, medium and dense conditions. The description and results of the tests can be found in (Davidson et al., 2019) and results are depicted in Figure 12(a). The corresponding physical (buoyant density γ') and strength (peak friction angle ϕ_p, the critical state friction angle ϕ_{crit} and the soil steel critical state friction angle δ_{crit}) soil parameters are given in Table 2 and were determined as a function of the relative density (Al-Defae et al., 2013). The dilatancy angle can be obtained from the peak and critical friction angles as per Bolton (1986) and Schanz and Vermeer (1996).

Centrifuge CPT tests used as the basis of this parametric study were compared in Figure 12 to field data, to ensure their similarity to real offshore soil conditions. The field tests reported in (Merritt et al., 2012), are representative of the Borkum West II offshore wind farm, installed in Germany. The soil conditions were characterised by medium-dense to very dense layers of sand. CPT results from (Chow, 1997) are representative of the Dunkirk site (estimated relative

14

density equal to 75% below 3m depth), extensively used for pile research testing since the 1980's and recently used for the PISA project (Byrne et al., 2017).

The field CPT results are more variable than the centrifuge tests, however they are in relatively good agreement with the dense centrifuge CPT results, while the medium dense centrifuge results describe a lower bound of the field results. The peak friction angle corresponding to the CPT data were estimated through the following empirical relationship (Knappett and Craig, 2012; Mayne, 2007)

$$\phi_p = 6.6 + 11 \log\left(\frac{q_c}{\sqrt{\sigma'_{v,0}}}\right) \tag{13}$$

where q_c is the cone resistance measured by the CPT and $\sigma'_{v,0}$ is the initial vertical effective stress.

Figure 12(b) shows that the interpreted peak friction angle for the centrifuge tests corresponds well to the parameters given in Table 2, that were calibrated based on oedometric and simple shear test by (Al-Defae et al., 2013) for a large range of relative densities. In addition, the peak friction angles interpreted from the field tests lie between the medium-dense and dense soil states considered in this parametric study.
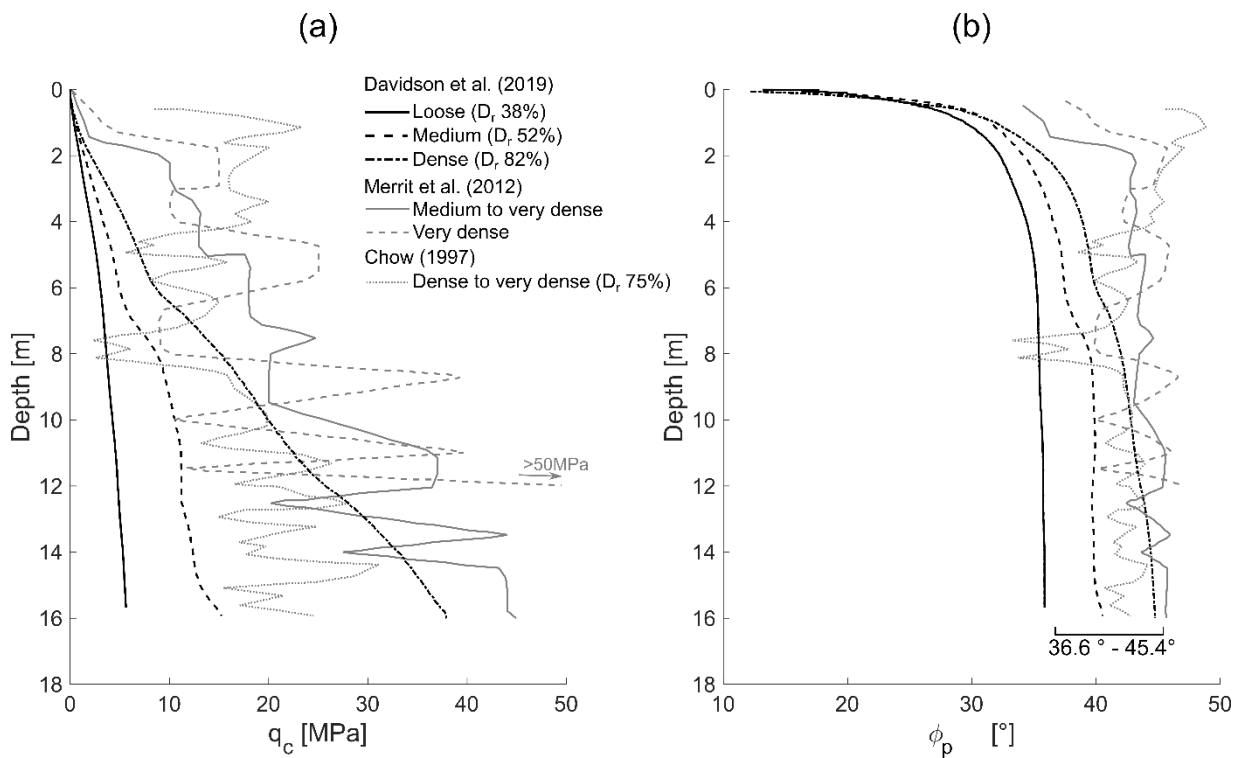

Figure 12 (a) Comparison of CPT tests undertaken in the centrifuge (Davidson et al., 2019) with field CPT results (Chow, 1997; Merritt et al., 2012). (b) Interpretation of the CPT tests as a peak friction angle ϕ_p after Eq. (13)

	D_r 38%	D_r 52%	D_r 82%
ϕ_p [°]	36.6	39.4	45.4
ϕ_{crit} [°]	32	32	32
ψ_p [°]	5.5	9	16.5
δ_{crit} [°]	24	24	24
γ' [kN/m³]	9.67	9.93	10.47

Table 2 Sand properties used for three relative densities, after (Al-Defae et al., 2013)

For completeness, two additional parameters are required to calculate the installation requirements in section 3.2. The CPT friction ratio F_r and CPT-soil friction angle, used to derive the stress drop index a (Lehane et al., 2005), were 0.01 and 18° respectively. The steel yield limit f_y was assumed to be 350MPa for the core, the helix and the welded joint.

4.3. Maximum capacity for a given geometry and installation torque

Figure 13 illustrates how the different structural and geotechnical constraints restrict the maximum embedment depth that can be achieved for a given geometry. The soil parameters used are those reported in Table 2 and Figure 12 for the dense sand case (D_r =82%). The geometry variables for this example are: D_h = 1.7m, D_h/D_c = 2, t_h = 0.1m. The maximum torque used for this example is equal to 7MNm and corresponds to the torque that could be applied onshore by a large casing rotator (Leffer, 2019).

The installation requirements (crowd force $F_{y,c}$ and torque) and uplift capacity (F_u) are all non-linear functions of the embedment depth. The torque requirement is depicted in Figure 13(a) and the installation torque, equal to 7MNm for this example, is not the limiting constraint in this case. The uplift capacity F_u and the crowd force $F_{y,c}$ are shown in Figure 13(b). The uplift capacity is constrained by the relative embedment ratio (assumed to be lower than 8) while the crowd force must be lower than the critical buckling force $F_{y,cr}$, i.e. the compression load for which buckling occurs. None of these conditions is the limiting constraint in this example. The evolution of the equivalent stress within the core during installation $\sigma_{eq,c}$, the bending stress inside the helix plate σ_x and the equivalent stress inside the weld joint $\sigma_{eq,w}$ are depicted in Figure 13(c). They all must be lower than the yield strength f_y. In this case, the plate bending is the limiting constraint that determines the maximum embedment depth (H_{max}).
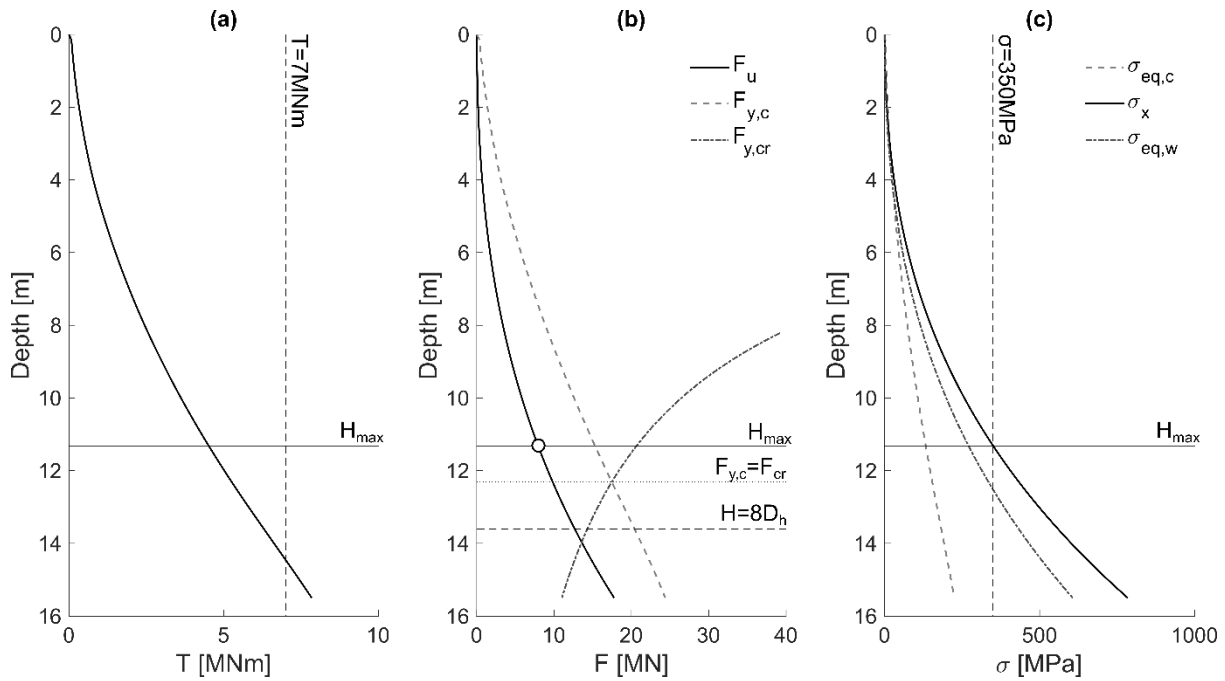
Figure 13 Determination of the maximum embedment (H_{max}) and uplift capacity of a screw anchor embedded in a dense sand for a given geometry (D_h=1.7m, D_h/D_c = 2, t_h = 0.1m). (a) Installation torque T, (b) Uplift capacity F_u, crowd force $F_{y,c}$, critical buckling force F_{cr} (c) equivalent stress within the core during installation $\sigma_{eq,c}$, stress due to bending in the plate σ_x, equivalent stress within the weld throat $\sigma_{eq,w}$.

4.4. Optimal design for a given available installation torque

The maximum uplift capacity corresponding to a given geometry can be calculated as exemplified in the previous section. Figure 14 depicts how this capacity evolves for all the geometries considered (varying D_h and D_h/D_c), whilst keeping the maximum torque T_{max} constant.

For the lower helix diameters, the limiting constraint is the maximum relative embedment ratio (H=8D_h) to ensure a shallow failure mode and limited displacement to reach capacity. Helix diameters lower than 0.5m are those frequently encountered for onshore applications. For such low helix diameters, the structural constraints are never limiting.

For the lower D_h/D_c ratios (=4 or 5), the limiting factor becomes the buckling constraint, as the core section is very small. As the helix diameter increases, the bending of the helix limits the uplift capacity. For the larger core diameters (D_h/D_c = 1.5 or 1.25), the maximum torque available limits the helix embedment and consequently decreases the available uplift capacity. The uplift capacity related to the geometry used as an example in the previous section is indicated in Figure 14. This geometry provides a large capacity, but it is possible to find another 'optimal' configuration whose capacity is larger. This configuration has a helix diameter D_h equal to 1.5m and a D_h/D_c ratio equal to 1.5. The total uplift capacity is equal to 8.7MN.
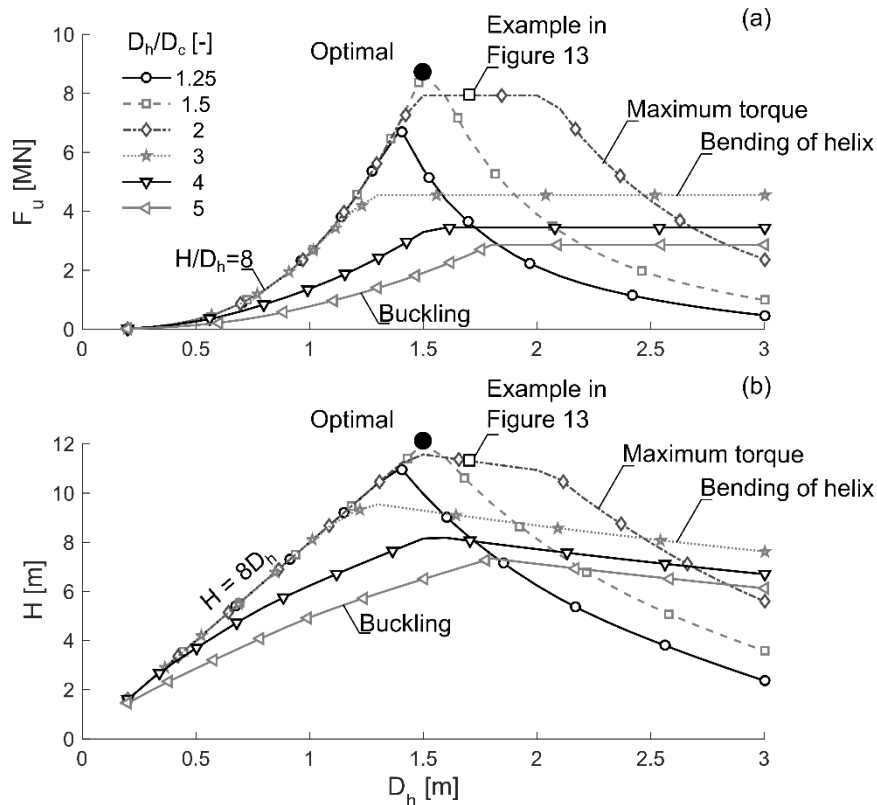
17

Figure 14 (a) Uplift capacity F_u and (b) embedment depth H of a screw anchor embedded in dense sand as a function of the helix diameter D_h and D_h/D_c ratio, assuming a maximum installation torque equal to 7MNm.

4.5. Optimal design for varying available installation torque

It is possible to identify the optimal configuration (D_h, D_h/D_c, H) corresponding to each maximum installation torque available, as shown in the previous section. This procedure is carried out for the three densities considered. The evolution of this maximum capacity and the corresponding optimal geometry as a function of the maximum torque is depicted in Figure 15.

The uplift capacity increases with the maximum torque available, as the anchor can be embedded to a greater depth H with a larger helix diameter D_h, as depicted in Figure 15(a,c,d). On the contrary, the corresponding helix to core diameter ratio D_h/D_c is decreasing, because the increasing uplift capacity generates a larger moment at the helix core connection, and consequently a larger bending stress at this point. Surprisingly, the maximum uplift capacity achievable is greater in loose than in dense sand, as shown in Figure 15(a). The lower strength properties of the loose material are compensated by the fact that the helix can be embedded to a greater depth for a given available torque. In contrast, there is no such difference in capacity between medium and dense properties, although the embedment depth is greater for the medium density sand. In this case, larger embedment depths in medium dense sand and compensated by a lower sand strength (with respect to the dense sample).

The uplift capacity of a screw anchor corresponding to current onshore installation technology ($T \leq 7$MNm) can reach up to 8.7-14.9MN in dense and loose sand respectively. This order of magnitude is largely sufficient for aquaculture applications (Figure 1), but it also proves that the screw anchor technology would be a good candidate to anchor wave energy converters (WEC). The use of screw anchors for larger tension-leg platforms (TLP) applications would require the development of large installation devices that can provide higher torque and potentially the use of several tendons and anchors per fairlead to reduce the required capacity per anchor. The maximum inclination of TLP tendons and possible interaction between adjacent anchors (Zhang et al., 2019) would then create additional constraints, e.g. the

18

anchors must be sufficiently spaced to avoid any interaction and reduction of their uplift capacity. It should be noted though that these constraints are based upon uplift capacity for an anchor having a shallow (uplift wedge) type failure mechanism. If future work is able to quantify the failure mechanism of more deeply embedded anchors, the range of application may be extended.
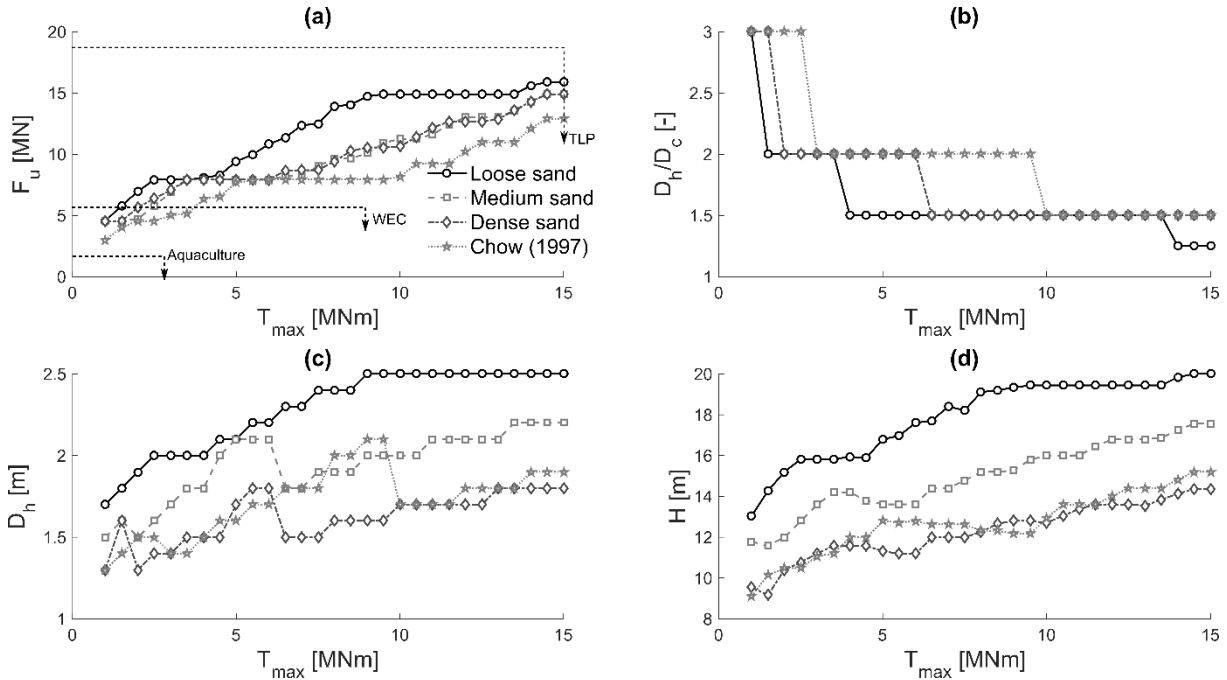

Figure 15 (a) Maximum uplift capacity and (b-c) geometry of the anchor as a function of the maximum torque applicable during installation T_{max} and soil conditions.

5. CASE STUDY

To highlight the relative performance of screw anchors compared to conventionally installed pile anchors the design procedure has been applied to the Dunkirk site test, which is a well-documented driven pile test site for which CPT tests (given in Figure 12(a), (Chow, 1997)) and soil characterisation is available (Aghakouchak, 2015; Zdravkovic et al., 2019). The relative soil density was reported to be equal to 75% on average from a depth of 3m (Chow, 1997). The strength properties of the soil are relatively homogeneous over the soil layer, as reported in Figure 12(b). Consequently, averaged parameters are used to calculate the uplift capacity of the anchor from Eq. (7). The parameters used are given in Table 3. The peak friction angle was deduced from Figure 12(b). The critical state friction angle, corresponding to triaxial compression, was selected as the critical state friction angle given in (Zdravkovic et al., 2019). The peak dilatancy angle was calculated according to (Schanz and Vermeer, 1996).

Results for this case study are compared in Figure 15 with those of the parametric study. The large cone tip resistance recorded close to the surface (ranging between 10 and 20MPa) together with a lower peak friction and dilatancy angles lead to slightly lower uplift capacity for the case study. Indeed, the large cone tip resistance induces more torque and force installation requirement, limiting the embedment depth, while the lower peak strength directly affects the peak capacity.

19

	D_r 75%
ϕ_p [°]	42
ϕ_{crit} [°]	32
ψ_p [°]	12.5
δ_{crit} [°]	24
δ_f [°]	29
γ' [kN/m³]	10.0

Table 3 Properties of the Dunkirk sand considered for the case study deduced from (Aghakouchak, 2015; Yang et al., 2016; Zdravković et al., 2015)

The efficiency of screw anchors is demonstrated by comparison with driven piles in Figure 16 for the Dunkirk case study. The calculated uplift capacity of driven piles is based on the UWA-05 method (Lehane et al., 2005), the CPT test data provided in Figure 12(a) and the properties given in Table 3. The thickness to diameter ratio of the driven piles t/D_c was assumed equal to 45 (Merritt et al., 2012). The sand-steel friction angle used to calculate the driven pile capacity was equal to 29°, as discussed in (Yang et al., 2016). Field pile load tests of tension piles in Dunkirk sand were added to the figure and are consistent with the results of the UWA-05 method.

To ensure a meaningful comparison with driven piles, the uplift capacity of screw anchors was calculated by varying their core diameter (at a fixed helix to core diameter ratio D_h/D_c equal to two) and calculating their maximum embedment depth. The maximum torque available for installation was assumed equal to 7MNm.

At very low embedment depths, the driven piles are more efficient than the screw anchors in this specific case. This is due to the large cone tip resistance which is directly used in the UWA-05 method to calculate the shear strength available along the pile shaft. The screw anchors become more efficient as the embedment increases. At an identical core diameter, the uplift capacity of a screw anchor is always larger than its straight pile counterpart for embedment larger than 6m. The maximum screw anchor capacity obtained (D_c = 0.75m) is equal to 6.35MN. Mobilising the same capacity would require a straight pile of twice this diameter and 40% longer, which would also need to be installed by driving (with the attendant noise and vibration). The limiting factor for this anchor is the conditions of maximum relative embedment depth (H/D_h =8). Consequently, greater depth and larger capacity could be obtained with this anchor size, providing a reliable simplified approach allows its estimation.

The three straight pile field tests reported in (Yang et al., 2016) are also compared to screw anchor designs (D_c = 0.5m, D_h/D_c = 2, variable length H) providing the same uplift capacity. Their respective dimensions are given in Table 4. In all cases, the screw anchor design is shorter and lighter than its straight pile counterpart. Consequently, the use of screw anchors requires a lower amount of steel (reduced embodied carbon) and their shorter/lighter design potentially make them easier to handle. In addition, they can be used in locations where the surface sediment is relatively thin over underlying rock.
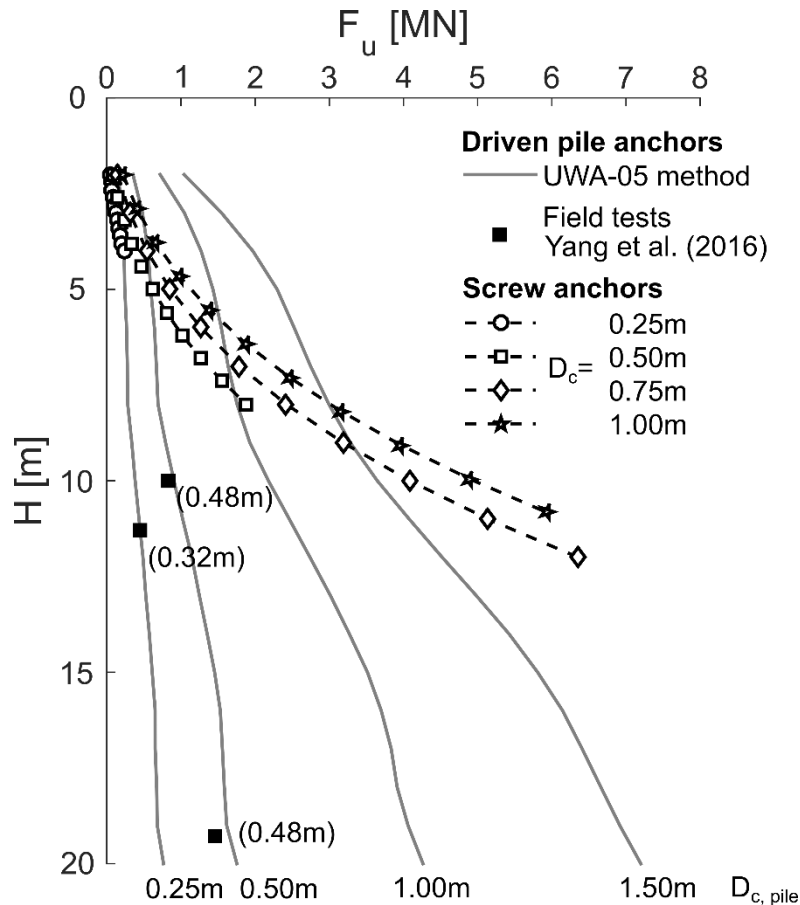
Figure 16 Comparison of the uplift capacity F_u provided by screw anchors (this paper methodology, core diameter D_c = 0.25, 0.50, 0.75 and 1.00, D_h/D_c = 2, T_{max} = 7MNm) and driven piles (UWA-05 pile design method, (Lehane et al., 2005) or field tests (Yang et al., 2016)) as a function of their embedment depth H for the Dunkirk sand case study based on CPT data provided by (Chow, 1997). The pile diameter for field tests is indicated in parentheses.

	F_u [MN]	0.444	0.82	1.45
Pile	H [m]	11.3	10.0	19.3
	D_c [mm]	322.0	457.0	457.0
	t_c [mm]	12.7	13.5	13.5
	W [t]	1.09	1.47	2.83
Screw	H [m]	4.3	5.6	7.2
	D_c [mm]	500.0	500.0	500.0
	t_c [mm]	12.0	13.0	12.0
	W [t]	0.73	0.96	1.31

Table 4 Comparison of dimensions (H, D_c, t_c) and weight W of field-tested driven piles (Yang et al., 2016) and screw anchors embedded in Dunkirk sand of identical uplift capacity F_u

The designed screw anchors are more efficient than straight piles under tension but could be further improved. The optimisation of anchor geometries (e.g. variable core diameter (Davidson et al., 2019) or pointed tips) or installation techniques (e.g. overflighting) could reduce the installation torque and force requirements. The use of a higher steel grade (e.g. f_y = 550MPa) could expand the design envelope by reducing the impact of the bending strength constraint. However, the current fabrication capabilities are likely to be another limiting factor (available geometries, welding of the helix), which depends on the available supply chain.

Several features could be added to the methodology to correspond to more specific cases or take into account operational conditions. Considering double helix screw anchors would reduce the helix bending constraint and increase initial stiffness, as the uplift capacity would be split between the two helices. However, this would increase the torque requirement and modify the uplift capacity criterion and be more complicated/costly to fabricate.

Incorporating cyclic loading and fatigue effects seems necessary in the future to consider more realistic in-service environmental offshore conditions. Although recent studies have begun to investigate some of these effects (Cerato and Victor, 2009; Lesny and Uchtmann, 2019; Newgard et al., 2015; Schiavon et al., 2017, 2016), no simplified analytical model is available to date to be incorporated within the proposed design methodology. The complex behaviour of screw anchors (e.g. accumulation of vertical displacement, structural load distribution modifications) while cyclically loaded is not well characterised to date and requires further fundamental research.

Finally, the very large anchor resistance required by Tension-Leg Platforms would necessitate the use of several anchors installed close to each other, introducing additional constraints (reduced group capacity or minimum separation distance) in the optimisation procedure.

6. CONCLUSION

The methodology presented in this paper integrates geotechnical and structural constraints into a single procedure to allow a rapid estimation of the maximum capacity of screw anchors and the optimisation of their geometry. It is based on several simplified approaches to consider the installation requirements (force and torque), the uplift capacity and the structural resistance (core torsion and buckling, plate bending, weld joint) of the anchor.

The performance envelopes defined in a parametric study show that screw anchors can provide a significant ultimate monotonic uplift capacity in sand over a range of densities, able to meet the needs of aquaculture, wave energy converters or floating wind. Although the reduction of noise and vibrations during installation was one of the main incentives for their development, screw anchors were proven to be more efficient than driven piles in tension for a specific case study in Dunkirk sand. Shorter and lighter anchors have other advantages such as a lower steel consumption and the ability to be installed in thinner layers of sand. However, their deployment offshore would require the development of powerful installation devices to achieve the targeted maximum torque (and crowd force).

The performance envelope of screw anchor capacities as presented is obviously limited to the hypotheses that were made. The anchor capacity could be further improved by selecting a larger steel grade or modifying the anchor geometry to reduce the installation force and torque requirements. The procedure could be further enhanced by incorporating a more sophisticated global buckling model, some displacement-based constraints or cyclic induced effects, although in this latter case further research is required to develop suitable simplified models.

7. ACKNOWLEDGEMENT

8. REFERENCES

Aghakouchak, A., 2015. Advanced laboratory studies to explore the axial cyclic behaviour of driven piles. Imperial College, UK.

Al-Baghdadi, T., 2018. Screw piles as offshore foundations : Numerical and physical modelling. PhD Thesis, University of Dundee, UK.

Al-Baghdadi, T.A., Brown, M.J., Knappett, J.A., Al-Defae, A.H., 2017a. Geotechnical engineering effects of vertical loading on lateral screw pile performance. Proc. Inst. Civ. Eng. Geotech. Eng. 170, 259–272. https://doi.org/10.1680/jgeen.16.00114

Al-Baghdadi, T.A., Davidson, C., Brown, M.J., Knappett, J.A., Brennan, A., Augarde, C., Coombs, W., Wang, L., 2017b. CPT based design procedure for installation torque prediction for screw piles installed in sand. 8th Int. Conf. Offshore Site Investig. Geotech. 346–353.

Al-Defae, A.H., Caucis, K., Knappett, J.A.A., 2013. Aftershocks and the whole-life seismic performance of granular slopes. Géotechnique 63, 1230–1244. https://doi.org/10.1680/geot.12.P.149

Aubeny, C., 2017. Geomechanics of Marine Anchors, First. ed. CRC Press, Boca Raton, Florida, USA.

Azcona, J., Palacio, D., Munduate, X., González, L., Nygaard, T.A., 2017. Impact of mooring lines dynamics on the fatigue and ultimate loads of three offshore floating wind turbines computed with IEC 61400-3 guideline. Wind Energy 20, 797–813. https://doi.org/10.1002/we.2064

Bachynski, E.E., Moan, T., 2014. Ringing loads on tension leg platform wind turbines. Ocean Eng. 84, 237–248. https://doi.org/10.1016/j.oceaneng.2014.04.007

Bachynski, E.E., Moan, T., 2012. Design considerations for tension leg platform wind turbines. Mar. Struct. 29, 89–114. https://doi.org/10.1016/j.marstruc.2012.09.001

Bjerrum, L., 1973. Geotechnical problems involved in foundations of structures in the North Sea. Géotechnique 23, 319–358. https://doi.org/10.1680/geot.1973.23.3.319

Bolton, M.D., 1986. The strength and dilatancy of sands. Géotechnique 36, 65–78. https://doi.org/10.1680/geot.1986.36.1.65

Burd, H.J., Taborda, D.M., Zdravković, L., Abadie, C.N., Byrne, B.W., Houlsby, G.T., Gavin, K.G., Igoe, D., Jardine, R.J., Martin, C.M., McAdam, R., Pedro, A.M., Potts, D.M., 2019. PISA design model for monopiles for offshore wind turbines : application to a marine sand. Géotechnique. https://doi.org/https://doi.org/10.1680/jgeot.18.P.277

Byrne, B., McAdam, R., Burd, H., Houlsby, G., Martin, C., Beuckelaers, W., Zdravkovic, L., Taborda, D., Potts, D., Jardine, R., Ushev, E., Liu, T., Abadias, D., Gavin, K., Igoe, D., Doherty, P., Skov Gretlund, J., Pacheco Andrade, M., Muir Wood, A., Schroeder, F., 2017. PISA: New Design Methods for Offshore Wind Turbine Monopiles, in: International Conference on Offshore Site Investigations and Geotechnics. London, UK.

Byrne, B.W., Houlsby, G.T., 2015. Helical piles: an innovative foundation design option for offshore wind turbines. Philos. Trans. R. Soc. A Math. Phys. Eng. Sci. 373, 1–11. https://doi.org/10.1098/rsta.2014.0081

Cerato, A.B., Victor, R., 2009. Effects of Long-Term Dynamic Loading and Fluctuating Water Table on Helical Anchor Performance for Small Wind Tower Foundations. J. Perform. Constr. Facil. 23, 251–261. https://doi.org/10.1061/(ASCE)CF.1943-5509.0000013

Cerfontaine, B., Brown, M.J., Knappett, J.A., Davidson, C., 2019a. Finite element modelling of the uplift behaviour of screw piles in sand, in: First International Symposium on Screw Piles for Energy Applications. Dundee, UK, pp. 69–75. https://doi.org/10.20933/100001123

Cerfontaine, B., Knappett, J., Brown, M.J., Davidson, C., Al-Baghdadi, T., Brennan, A., Augarde, C., Coombs, W., Wang, L., Blake, A., Richards, D., Ball, J., 2020. A Finite Element approach for determining the full load-displacement relationship of axially-loaded screw anchors, incorporating installation effects. (Accepted Publ. in) Can. Geotech. J.

Cerfontaine, B., Knappett, J.A., Brown, M.J., Bradshaw, A.S., 2019b. Effect of soil deformability on the failure mechanism of shallow plate or screw anchors in sand.

23

Comput. Geotech. 109, 34–45. https://doi.org/https://doi.org/10.1016/j.compgeo.2019.01.007

Chow, F.C., 1997. Investigations into the behaviour of displacement piles for offshore foundations. Imperial College.

Clemence, S.P., Lutenegger, A.J., 2015. Industry survey of state of practice for helical piles and tiebacks. DFI J. 9, 21–41. https://doi.org/10.1179/1937525514Y.0000000007

Davidson, C., Al-Baghdadi, T., Brown, M., Brennan, A., Knappett, J., Augarde, C., W., C., Wang, L., Richards, D., Blake, A., Ball, J., 2018a. A modified CPT based installation torque prediction for large screw piles in sand, in: Hicks, M., Pisanò, F., Peuchen, J. (Eds.), Cone Penetration Testing. Delft, The Netherlands. https://doi.org/https://doi.org/10.1201/9780429505980

Davidson, C., Al-Baghdadi, T., Brown, M.J., Brennan, A., Knappett, J.A., Augarde, C., Coombs, W., Wang, L., Richards, D.J., Blake, A., Ball, J., 2018b. Centrifuge modelling of screw piles for offshore wind energy foundations, in: Proceedings of the 9th International Conference on Physical Modelling in Geotechnics (ICPMG 2018). London, UK, pp. 695–700.

Davidson, C., Brown, M.J., Brennan, A.J., Knappett, J.A., Cerfontaine, B., Sharif, Y.U., 2019. Physical modelling of screw piles for offshore wind energy, in: Davidson, C., Brown, M.J., Knappett, J.A., Brennan, A.J., Augarde, C., Coombs, W., Wang, L., Richards, D., White, D.J., Blake, A. (Eds.), First International Symposium on Screw Piles for Energy Applications. University of Dundee, Dundee, UK. https://doi.org/10.20933/100001123

Davidson, C., Brown, M.J., Cerfontaine, B., Al-Baghdadi, T., Knappett, J., Brennan, A., Augarde, C., Coombs, W., Wang, L., Blake, A., Richards, D., Ball, J., 2020. Physical modelling to demonstrate the feasibility of screw piles for offshore jacket supported wind energy structures. (submitted Consid. in) Géotechnique.

Deeks, A.D., White, D.J., Ishihara, Y., 2010. Novel piling:Axial and rotary jacking, in: 11th International Conference of the Deep Foundations Institute. London, UK, p. 24.

DNV-GL, 2018. DNVGL-ST-0119 Floating wind turbine structures.

El Sharnouby, M.M., El Naggar, M.H., 2012. Field investigation of axial monotonic and cyclic performance of reinforced helical pulldown micropiles. Can. Geotech. J. 49, 560–573. https://doi.org/10.1139/t2012-017

EN1193-1-8, 2005. Eurocode 3: Design of steel structures - Part 1-8: Design of joints Eurocode. Brussels, Belgium.

Eurocode, E.C. for standardization, 2005. Eurocode 3: Design of steel structures - Part 1-1: General rules and rules for buildings. Brussels, Belgium.

Fontana, C.M., S., H., Arwade, S.R., DeGroot, D.J., Landon, M.E., Aubeny, C.P., Diaz, B., Myers, A.T., Ozmutlu, S., Hallowell, S.T., Arwade, S.R., DeGroot, D.J., Landon, M.E., Aubeny, C.P., Diaz, B., Myers, A.T., Ozmutlu, S., Melissa, E., Hallowell, S.T., Andrew, T., DeGroot, D.J., Charles, P., Ozmutlu, S., 2018. Multiline anchor force dynamics in floating offshore wind turbines. Wind Energy 21, 1177–1190. https://doi.org/10.1002/we.2222

Gabr, M.A., Wang, J.J., Zhao, M., 1997. Buckling of Piles with General Power Distribution of Lateral Subgrade Reaction. J. Geotech. Geoenvironmental Eng. 123, 123–130. https://doi.org/10.1061/(asce)1090-0241(1997)123:2(123)

Gaudin, C., O'Loughlin, 2018. Geotechnical modelling for offshore renewables, in: Proceedings of the 9th International Conference on Physical Modelling in Geotechnics (ICPMG 2018). London, UK, pp. 33–41.

Ghaly, A., Hanna, A., Hanna, M., 1991. Installation torque of screw anchors in dry sand. Soils Found. 31, 77–92.

Giampa, J., Bradshaw, A., Schneider, J., 2017. Influence of Dilation Angle on Drained Shallow Circular Anchor Uplift Capacity. Int. J. Geomech. 17, 4016056. https://doi.org/10.1061/(ASCE)GM.1943-5622.0000725

Giken, 2018. Silent Piler [WWW Document]. URL https://www.giken.com/en/products/silent_piler/ (accessed 10.18.18).

Han, Y., Le, C., Ding, H., Cheng, Z., Zhang, P., 2017. Stability and dynamic response analysis of a submerged tension leg platform for offshore wind turbines. Ocean Eng. 129, 68–82.

https://doi.org/10.1016/j.oceaneng.2016.10.048

Hao, D., Wang, D., O'Loughlin, C.D., Gaudin, C., O'Loughlin, C.D.C.D., Gaudin, C., 2019. Tensile monotonic capacity of helical anchors in sand: interaction between helices. Can. Geotech. J. 56, 1534–1543. https://doi.org/10.1139/cgj-2018-0202

Harnish, J., Naggar, H.E.H.E.H. El, El Naggar, H., 2017. Large Diameter Helical Pile Capacity - Torque Correlations. Can. Geotech. J. 986, 1–51. https://doi.org/https://doi.org/10.1139/cgj-2016-0156

Heelis, M.E., Pavlovic, M.N., West, R.P., Pavlović, M.N., West, R.P., 2004. The analytical prediction of the buckling loads of fully and partially embedded piles. Geotechnique 54, 363–373. https://doi.org/10.1680/geot.2004.54.6.363

Herduin, M., Gaudin, C., Johanning, L., 2018. Anchor sharing in sands: centrifuge modelling and soil element testing to characterise multi-directional loadings, in: Proceedings of the ASME 2018 37th International Conference on Ocean, Offsore and Artic Engineering, OMAE. Madrid, Spain.

Hong-yan, D., Le, W., Zhang, P.-Y., C.-H., L., 2018. Study on the lateral bearing capacity of single-helix pile for offshore wind power. Proc. ASME 2018 37th Int. Conf. Ocean. Offshore Artic Eng. 1–6.

Huang, C.C., Tang, H.J., Liu, J.Y., 2008. Effects of waves and currents on gravity-type cages in the open sea. Aquac. Eng. 38, 105–116. https://doi.org/10.1016/j.aquaeng.2008.01.003

Jaky, J., 1944. The coefficient of earth pressure at rest. J. Soc. Hungarian Archit. Eng. 78, 355–358.

Jardine, R.J., Hight, D.W., McIntosh, W., 1988. Hutton tension leg platform foundations of pile group axial load-displacement measurement relations. Géotechnique 38, 219–230.

JFE, 2019. JFE Steel corporation major building materials catalog [WWW Document]. URL http://www.jfe-steel.co.jp/en/products/list.html#! (accessed 3.16.19).

Knappett, J.A., Craig, F., 2012. Craig's soil mechanics.

Knappett, J.A.J.A., Caucis, K., Brown, M.J.M.J., Jeffrey, J.R.J.R., Ball, J.D.J.D., 2016. CHD pile performance: part II – numerical modelling. Proc. Inst. Civ. Eng. - Geotech. Eng. 169, 436–454. https://doi.org/10.1680/jgeen.15.00132

Le, C., Li, Y., Ding, H., 2019. Study on the Coupled Dynamic Responses of a Submerged Floating Wind Turbine under Different Mooring Conditions. Energies 12, 418. https://doi.org/10.3390/en12030418

Le, T.M.H., Eiksund, G.R., Strøm, P.J., Saue, M., 2014. Geological and geotechnical characterisation for offshore wind turbine foundations: A case study of the Sheringham Shoal wind farm. Eng. Geol. 177, 40–53. https://doi.org/10.1016/j.enggeo.2014.05.005

Leffer, 2019. Hydraulic casing rotator type RDM and RDM-M [WWW Document]. Broch. - RDM. URL http://www.lefferna.com/product/hydraulic-casing-rotators/ (accessed 9.10.19).

Lehane, B., Schneider, J., Xu, X., 2005. The UWA-05 method for prediction of axial capacity of driven piles in sand, in: Gourvenec, S., Cassidy, M. (Eds.), Frontiers in Offshore Geotechnics: ISFOG. Perth, Asutralia, pp. 683–689. https://doi.org/10.1201/noe0415390637.ch76

Lesny, K., Uchtmann, M., 2019. Suitability of helical anchors for mooring wave energy converting system, in: Proceedings of the 1st Vietnam Symposium on Advances in Offshore Engineering. Springer Singapore, pp. 498–503. https://doi.org/10.1007/978-981-13-2306-5

Li, W., Zhang, D.J.Y., Sego, D.C., Deng, L., 2018. Field Testing of Axial Performance of Large-Diameter Helical Piles at Two Soil Sites. J. Geotech. Geoenvironmental Eng. 144, 06017021. https://doi.org/10.1061/(ASCE)GT.1943-5606.0001840.

Malik, A.A., Kuwano, J., Tachibana, S., Maejima, T., 2019. Effect of helix bending deflection on load settlement behaviour of screw pile. Acta Geotech. 0123456789. https://doi.org/10.1007/s11440-019-00778-x

Matha, D., 2009. Model Development and Loads Analysis of an Offshore Wind Turbine on a Tension Leg Platform, with a Comparison to Other Floating Turbine Concepts Thesis

Supervisors. Universität Stuttgart.

Mayne, P., 2007. Cone penetration testing: A synthesis of highway practice. NCHRP Synthesis Report 368. Washington DC.

Merritt, A.S., Schroeder, F.C., Jardine, R.J., Stuyts, B., Cathie, D., Cleverly, W., 2012. Development of Pile Design Methodology for an Offshore Wind Farm in the North Sea, in: Proceedings of the 7th International Conference of Offshore Site Investigations and Geotechnics. Society of Underwater Technology, London, UK.

Meyerhof, G.G., Adams, J.I., 1968. The ultimate uplift capacity of foundations. Can. Geotech. J. 5, 225–244.

Mitsch, M.P., Clemence, S.., 1985. The uplift capacity of helix anchors in sand, in: Uplift Behavior of Anchor Foundations in Soil. Proceedings of the ASCE. New-York, USA, pp. 26–47.

Negro, V., López-Gutiérrez, J.S., Esteban, M.D., Alberdi, P., Imaz, M., Serraclara, J.M., 2017. Monopiles in offshore wind: Preliminary estimate of main dimensions. Ocean Eng. 133, 253–261. https://doi.org/10.1016/j.oceaneng.2017.02.011

Newgard, J.T., Schneider, J. a., Thompson, D.J., 2015. Cyclic response of shallow helical anchors in a medium dense sand, in: Frontiers in Offshore Geotechnics III. Taylor & Francis Group, London, Oslo, Norway, pp. 913–918. https://doi.org/10.1201/b18442-131

Oguz, E., Clelland, D., Day, A.H., Incecik, A., López, J.A., Sánchez, G., Almeria, G.G., 2018. Experimental and numerical analysis of a TLP floating offshore wind turbine. Ocean Eng. 147, 591–605. https://doi.org/10.1016/j.oceaneng.2017.10.052

Papadopoulou, K., Saroglou, H., Papadopoulos, V., 2014. Finite Element Analyses and Experimental Investigation of Helical Micropiles. Geotech. Geol. Eng. 32, 949–963. https://doi.org/10.1007/s10706-014-9771-6

Perko, H.A., 2009a. Helical Piles: A practical Guideto Design and Installation, First Edit. ed. John Wiley & Sons.

Perko, H.A., 2009b. Helical Piles: A Practical Guide to Design and Installation, 1st Edit. ed. John Wiley & Sons. https://doi.org/10.1002/9780470549063

Pisano, F., di Prisco, C., 2014. Numerical modeling and mechanical analysis of an innovative soil anchoring system. Acta Geotech. 9, 1013–1028. https://doi.org/10.1007/s11440-013-0250-7

PLAXIS, 2017. PLAXIS 2D Reference Manual. Delft, The Netherlands.

Randolph, M., Cassidy, M., Gourvenec, S., Erbrich, C., 2005. Challenges of offshore geotechnical engineering Les défis de la géotechnique offshore, in: Proceedings of the International Conference on Soil Mechanics and Geotechnical Engineering ICSMGE. Balkema Publishers, Osaka, Japan.

Randolph, M., Gourvenec, S., 2011. Offshore Geotechnical Engineering, 1st Edit. ed. CRC Press, London.

Sakr, M., 2009. Performance of helical piles in oil sand. Can. Geotech. J. 46, 1046–1061. https://doi.org/10.1139/T09-044

Schanz, T., Vermeer, A., Bonnier, P., 1999. The hardening soil model: formulation and verification. Beyond 2000 Comput. Geotech. 10 years PLAXIS Int. Proc. Int. Symp. beyond 2000 Comput. Geotech. Amsterdam Netherlands 1820 March 1999 281.

Schanz, T., Vermeer, P.A., 1996. Angles of friction and dilatancy of sand. Géotechnique 46, 145–151.

Schiavon, J.A., Tsuha, C.H.C., Neel, A., Thorel, L., Schiavon, J.A., 2016. Centrifuge modelling of a helical anchor under different cyclic loading conditions in sand. Int. J. Phys. Model. Geotech. https://doi.org/10.1680/jphmg.17.00054

Schiavon, J.A., Tsuha, C.H.C., Thorel, L., 2017. Cyclic and post-cyclic monotonic response of a single-helix anchor in sand. Géotechnique Lett. 7, 11–17.

Sturm, H., 2017. Design Aspects of Suction Caissons for Offshore Wind Turbine Foundations, in: International Conference on Soil Mechanics and Geotechnical Engineering. pp. 45–63.

Timoshenko, S., Woinowky-Krieger, S., 1959. Theory of Plates and Shells, 2nd Edit. ed. McGraw-hill.

Tsuha, C.H.C., Aoki, N., 2010. Relationship between installation torque and uplift capacity of deep helical piles in sand. Can. Geotech. J. 47, 635–647. https://doi.org/10.1139/T09-128

Tsuha, C.H.C., Aoki, N., Rault, G., Thorel, L., Garnier, J., 2007. Physical modelling of helical pile anchors. Int. J. Phys. Model. Geotech. 494, 1–12.

Vicente, P.C., Falcão, A.F.O., Justino, P.A.P., 2013a. Nonlinear dynamics of a tightly moored point-absorber wave energy converter. Ocean Eng. https://doi.org/10.1016/j.oceaneng.2012.12.008

Vicente, P.C., Falcão, A.F.O., Justino, P.A.P., 2013b. Nonlinear dynamics of a tightly moored point-absorber wave energy converter. Ocean Eng. 59, 20–36. https://doi.org/10.1016/j.oceaneng.2012.12.008

White, D.J., Cheuk, C.Y., Bolton, M.D., 2008. The uplift resistance of pipes and plate anchors buried in sand. Géotechnique 58, 771–779. https://doi.org/10.1680/geot.2008.3692

Yang, Z., Jardine, R., Guo, W., Chow, F., 2016. A Comprehensive Database of Tests on Axially Loaded Piles Driven in Sand, A Comprehensive Database of Tests on Axially Loaded Piles Driven in Sand. Academic Press. https://doi.org/10.1016/c2015-0-01032-2

Yong-Sheng, Z., Xiao-he, S.H.E., Yan-ping, H.E., Jian-min, Y., Tao, P., Yu-feng, K.O.U., 2018. Experimental Study on New Multi-Column Tension-Leg-Type Floating. China Ocean Eng. 32, 123–131.

Zdravkovic, L., Jardine, R.J., Taborda, D.M., Abadias, D., Burd, H., Byrne, B., Gavin, K.G., Houlsby, G.T., Igoe, D., Liu, T., Martin, C.M., McAdam, R., Muir Wood, A., Potts, D., Gretlund, J.S., Ushev, E., 2019. Ground characterisation for PISA pile testing and analysis. Géotechnique. https://doi.org/https://doi.org/10.1680/jgeot.18.PISA.001

Zdravković, L., Taborda, D., Potts, D., Jardine, R., Sideri, M., Schroeder, F., Byrne, B., McAdam, R., Burd, H., Houlsby, G., Martin, C., Gavin, K., Doherty, P., Igoe, D., Wood, A., Kallehave, D., Gretlund, J., 2015. Numerical modelling of large diameter piles under lateral loading for offshore wind applications, in: Frontiers in Offshore Geotechnics III. Oslo, Norway, pp. 759–764. https://doi.org/10.1201/b18442-105

Zhang, X., Liu, J., Liu, M., 2019. Experimental study on uplift behavior of group anchors in sand. Geotech. Test. J. 42. https://doi.org/10.1520/GTJ20170430

Zienkiewicz, O.C., Taylor, R.L., 2000. The finite element method (vol. 2): Solid mechanics, Fifth Edit. ed, Vasa. Butterworth-Heineman, Oxford, UK.

9. NOTATION

A_h	Area of the helix
a	Stress drop index
a_w	Weld throat
D_c	Straight pile or screw anchor core diameter
D_h	Helix diameter
E	Young's modulus
F	Equivalent force in the welding joint such that $M = F\, t_h$
F_b	Penetration resistance of the pile base
F_c	Penetration resistance of the pile core
F_h	Penetration resistance of the helix
F_r	CPT friction ratio, typically close to 1%
F_{s1}, F_{s2}	Uplift factors
F_u	Ultimate axial uplift capacity
F_y	Axial uplift load
$F_{y,c}$	Vertical compression force (crowd force)
$F_{y,cr}$	Vertical compression critical elastic load (Euler buckling)
f_y	Steel yield limit
H	Straight pile or screw anchor embedment (helix position)
H_{max}	Maximum embedment depth of the screw anchor based on all constraints
I	Second moment of area of the screw anchor core
K	Buckling constant depending on boundary conditions
K_0	Coefficient of earth pressure at rest
k	Constant for the calculation of helix bending
M	Bending moment in the helix
p_h	Helix pitch
q_c	Cone tip resistance
$\bar{q}_c$	Averaged cone tip resistance
q	Distributed constant load acting on the helix
Q	Equivalent shear force acting on the welded joint
t_c	Straight pile or screw anchor core thickness
t_h	Helix thickness
u_y	Vertical uplift displacement
T	Torque applied at the top of the anchor
T_b	Torque created by the pile base
T_c	Torque created by the pile core
T_h	Torque created by the helix
W	Weight of the screw anchor or straight pile
γ'	Buoyant unit weight of the soil
δ_{crit}	Critical state soil-steel interface friction angle (screw anchor installation)
δ_f	Critical state soil-steel interface friction angle (driven pile)
θ	Helix angle
σ	Normal stress
σ_N'	Normal effective stress acting on the helix
$\sigma_{eq,c}$	Equivalent Von Mises stress acting on the core section
σ_{v0}'	Initial vertical effective stress
σ_x	Horizontal stress acting parallel to the helix due to the bending moment
σ_y	Vertical stress acting on the core section
τ	Shear stress
ϕ_{crit}	Critical state friction angle of the soil
ϕ_p	Peak friction angle of the soil
ψ_p	Peak dilatancy angle

10. APPENDIX: FORCE/TORQUE PREDICTION METHOD

The different components of the torque and force prediction method are calculated as per (Davidson et al., 2020). The core torque and vertical forces are calculated incrementally by summing up elementary pile core height (dH).

$$T_c = \sum a\bar{q}_c \tan\delta_{crit} \; dH \frac{D_c^2}{2} \tag{14}$$

$$T_b = \bar{q}_c \pi \frac{D_c^3}{12} \tan\delta_{crit} \tag{15}$$

$$T_h = a\bar{q}_c \frac{\tan(\delta_{crit} + \theta)\pi \left(D_h^3 - D_c^3\right)}{12 K_0} + a\bar{q}_c \frac{t_h \tan\delta_{crit}\, \pi D_h^2}{12} + a\,\bar{q}_c t_h \frac{D_h^2 - D_c^2}{4} \tag{16}$$

$$a = \frac{F_r}{\tan\delta_{crit}} \tag{17}$$

$$K_0 = 1 - \sin\phi_{crit} \tag{18}$$

$$\theta = \tan^{-1}\left(\frac{p_h}{\pi D_h}\right) \tag{19}$$

$$F_c = \sum 0.6\, a\bar{q}_c \tan\delta_{crit} \; dH \pi D_c \tag{20}$$

$$F_b = 0.6\, \bar{q}_c \pi \frac{D_c^2}{4} \tag{21}$$

$$F_h = a\bar{q}_c \frac{\pi \left(D_h^2 - D_c^2\right)}{4 K_0} + a\bar{q}_c \frac{t_h \pi D_h}{K_0} + \bar{q}_c t_h \frac{D_h - D_c}{2} \tag{22}$$

11. APPENDIX: WELD JOINT

The maximum stress in the helix section σ_x generated by the uniformly distributed surface load q is given by the following equation

$$\sigma_x = q \, k \, \frac{D_h^2}{4t_h^2} \qquad (23)$$

The bending moment at the helix to shaft connection is than obtained through

$$M = \sigma_x W_{el} \qquad (24)$$

where W_{el} is the elastic section modulus, equal to $t_h^2/6$ in this case. Similarly, the shear force at the connection can be obtained through

$$Q = \frac{q\frac{\pi}{4}\left(D_h^2 - D_c^2\right)}{\pi D_c} = \frac{qD_c}{4}(R_{hc}^2 - 1) \qquad (25)$$

where R_h is the ratio between the helix diameter D_h and the core diameter D_c. The bending moment in the helix section can be converted into two point charges *F* applied to the upper and lower weld joints such that

$$M = F \, t_h \qquad (26)$$

Subsequently, the normal σ_w and shear τ_w stress along the weld throat a_w is given by

$$\sigma_w = \frac{\left(F \pm \frac{Q}{2}\right)\cos 45}{a_w} \quad \& \quad \tau_w = \frac{\left(F \mp \frac{Q}{2}\right)\cos 45}{a_w} \qquad (27)$$

where the $\pm$ sign refers to the upper or lower wedge joint (tension or compression while uplifted). It is assumed the material obeys the Mises criterion, therefore the equivalent stress σ_{eq} is obtained through

$$\sigma_{eq,w} = \sqrt{\sigma_w^2 + 3\tau_w^2} \leq f_y \qquad (28)$$

where it is assumed that the welded joint has the same strength as the steel of the helix. Inserting Equation (27) into this equation leads to the definition of a maximum distributed load

$$q_{w,max} = \frac{f_y a_w}{\cos 45} \frac{1}{\sqrt{4\left[\left(\frac{\frac{k}{24}D_h^2}{t_h}\right)^2 + \left(\frac{D_c}{8}(R_{hc}^2 - 1)\right)^2\right] \mp \frac{k}{48}\frac{D_h^2}{t_h}D_c(R_{hc}^2 - 1)}} \qquad (29)$$

The relative embedment ratio that corresponds to this normal stress can be obtained by solving Eq. (7).